PHYSICAL REVIEW B **96**, 064525 (2017)

Transport properties of ultrathin $YBa_2Cu_3O_{7-\delta}$ nanowires: A route to single-photon detection

Riccardo Arpaia,[1] Dmitri Golubev,[2] Reza Baghdadi,[1] Regina Ciancio,[3] Goran Dražić,[4] Pasquale Orgiani,[5]
Domenico Montemurro,[1] Thilo Bauch,[1] and Floriana Lombardi[1,*]
[1]*Quantum Device Physics Laboratory, Department of Microtechnology and Nanoscience, Chalmers University of Technology, SE-41296 Göteborg, Sweden*
[2]*Low Temperature Laboratory (OVLL), Aalto University School of Science, P.O. Box 13500, FI-00076 Aalto, Finland*
[3]*CNR-IOM, TASC Laboratory, Area Science Park, Basovizza S.S. 14 km 163.5, I-34149 Trieste, Italy*
[4]*Laboratory for Materials Chemistry, National Institute of Chemistry, Hajdrihova 19, SI-1001 Ljubljana, Slovenia*
[5]*CNR-SPIN, University of Salerno, I-84084 Fisciano (SA), Italy*

(Received 8 October 2016; revised manuscript received 7 July 2017; published 25 August 2017)

We report on the growth and characterization of ultrathin $YBa_2Cu_3O_{7-\delta}$ (YBCO) films on MgO (110) substrates, which exhibit superconducting properties at thicknesses down to 3 nm. YBCO nanowires, with thicknesses down to 10 nm and widths down to 65 nm, have also been successfully fabricated. The nanowires protected by a Au capping layer show superconducting properties close to the as-grown films and critical current densities, which are limited by only vortex dynamics. The 10-nm-thick YBCO nanowires without the Au capping present hysteretic current-voltage characteristics, characterized by a voltage switch which drives the nanowires directly from the superconducting to the normal state. We associate such bistability to the presence of localized normal domains within the superconductor. The presence of the voltage switch in ultrathin YBCO nanostructures, characterized by high sheet resistance values and high critical current values, makes our nanowires very attractive devices to engineer single-photon detectors.

DOI: 10.1103/PhysRevB.96.064525

I. INTRODUCTION

Single-photon detectors based on superconducting nanowires (SNSPDs) [1] employ thin films with a thickness of a few atomic layers, in which the superconducting properties are well preserved after nanopatterning [2–4].

At present, only conventional superconductors like NbN, NbTiN, Nb, and WSi, in which reliable nanofabrication routines are well established, have been employed to realize such devices. $YBa_2Cu_3O_{7-\delta}$ (YBCO) and, more generally, high-critical-temperature superconductors (HTSs) are promising materials to use as SNSPDs since they meet all the crucial requirements for detection, such as a short coherence length $\xi = \hbar v_F/\pi\Delta$ (where v_F is the Fermi velocity and Δ is the superconducting gap) and, simultaneously, the highest possible transition temperature T_C [5–8]. However, the serious degradation of the superconducting properties, which typically occurs in HTS thin films when the thickness approaches the nanometer scale, is a crucial issue for the realization of nanoscale devices.

The growth of ultrathin YBCO films has been the object of intense research since the discovery of cuprate superconductors. Initially, the focus was on YBCO films a few (ideally one) unit cells thick, embedded between layers of $PrBa_2Cu_3O_{7-\delta}$ (PBCO), and the main systems under investigation, precursors of two-dimensional (2D) superconductors [9], were YBCO/PBCO superlattices [10,11] and PBCO/YBCO/PBCO trilayers structures [12,13].

The choice of using PBCO in combination with YBCO was initially made because of the peculiar PBCO properties, neither metallic nor superconducting, with a crystallographic structure and lattice parameters very similar to those of YBCO. PBCO has often been used as a protective layer since bare ultrathin YBCO films are characterized by degraded superconducting properties as a consequence of the surface and chemical instability of the compound [12]. However, the deposition at high temperature of a PBCO layer may also lead to some complications, such as the interdiffusion at the interface between PBCO and YBCO, which causes the substitution of Pr atoms in Y sites, with percentages as high as 30% [14]. It is known that a 45% atomic interdiffusion into the first YBCO layer results in a T_C of $\sim$30 K for the resulting alloy [9]. Hence, few-layer YBCO thin films are characterized by a reduced T_C.

In this paper we show the growth and characterization of ultrathin YBCO films on MgO (110) substrates, which exhibit superconductivity at thicknesses down to 3 nm. High-quality superconducting properties have been obtained using a Au film as a capping layer. Nanowires with widths down to 65 nm have also been realized on bare 10-nm-thick films and on films capped with Au. The YBCO nanowires without Au capping show a voltage switch in the current-voltage characteristics (IVCs), similar to that of NbN nanowires, which brings the system directly from the superconducting to the normal state. This feature, occurring in structures with high sheet resistance and high critical current density, makes our ultrathin ($\sim$10 nm) nanowires ideal candidates for ultrafast single-photon detection.

II. HTSs AS MATERIALS FOR SNSPDs

YBCO and HTSs in general are of great interest in the quest for new materials for SNSPDs. The high critical temperature, $T_C^{YBCO} \approx 90$ K, could broaden the ultralow-temperature range of operation (1.7–5 K) characterizing traditional SNSPDs made of low-critical-temperature superconductors (LTSs), such as NbN, NbTiN, and Nb. The coherence length, $\xi_0^{YBCO} \approx 2$ nm, which is comparable to that of traditional SNSPD

---

[*] floriana.lombardi@chalmers.se

materials, $\xi_0^{NbN} \approx 5$ nm [15], offers the possibility to squeeze the dimensions of the detecting elements down to several nanometers without entering in a regime dominated by phase fluctuations, where dark counts would play a big role [16,17]. HTS SNSPDs can also be interesting from a more fundamental physics point of view, offering new scenarios for intrinsic mechanisms involved in the formation of the photoresponse signal. In LTS SNSPDs, models based on vortex-assisted photon counting are nowadays the most commonly accepted to describe the detection process (although none of the models proposed so far has been able to describe all the experimental data) [4,18]. Superconductivity in HTS materials and nanostructures is, however, quite different from conventional superconductors: the role of vortices could, for example, be different as a consequence of the peculiar vortex dynamics characterizing this class of materials [19].

Several works have been devoted to the realization of YBCO nanowires for their application in single-photon detectors [20–22]: despite all this technological effort, a HTS SNSPD has still not been realized. The reason for this could lie in the different material properties of YBCO with respect to LTS materials, commonly used in SNSPDs.

LTS nanowires are commonly characterized by high critical current densities, hysteretic IVCs, and high sheet resistances. High critical current densities are required to improve the signal-to-noise ratios; the amplitude of the output signals is proportional to the superconductive critical current, which is limited by the small cross-sectional area of the wire. Hysteretic IVCs ensure the switching mechanism of a SNSPD as a consequence of the photon event. The presence of the hysteresis is very common in NbN nanostructures already at thicknesses $t = 50$ nm, much larger than those requested for their employment in SNSPDs (see Fig. 1). The hysteresis is a distinctive feature of the formation and development of a self-stabilizing hot spot in the superconducting wire [25,26], and it is a consequence of the low value of thermal conductivity in this material ($\kappa \approx 10^{-2}$–10^{-1} W m^{-1} K^{-1} in the normal state). Finally, high sheet resistance values make the nanowire resistance much higher than the external load resistance R_L (typically 50 Ω) in parallel with the device, thus favoring the redistribution of all the bias current into the readout line, where the signal appears. In NbN, this is commonly achieved using microcrystalline, granular, ultrathin films: the normal resistance R_N increases without reducing the homogeneity of the films, and nanodefects, acting as pinning centers, may even enhance the critical current density of the devices [27,28].

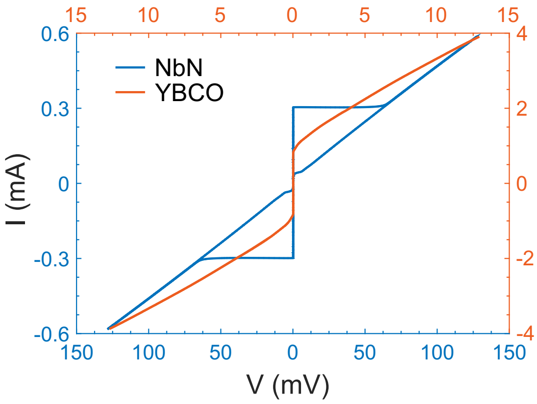

FIG. 1. Current-voltage characteristics at $T = 4.2$ K of a 50-nm-thick, 75-nm-wide, and 120-nm-long NbN nanowire (blue) and of a bare YBCO nanowire (orange) having the same dimensions. Both the nanowires have been realized following the nanopatterning procedure described in Refs. [23,24]. In NbN, a large-voltage switch, occurring just above the critical current, brings the whole nanowire into a state characterized by a differential resistance corresponding to the normal resistance R_N. In YBCO, a flux-flow behavior, characterized by differential resistances $\ll R_N$, dominates at currents higher than the critical one.

For an ideal YBCO-based SNSPD, the critical current density J_C should be as close as possible to the depairing/vortex entry limit, which equals $J_v \approx 8 \times 10^7$ A/cm^2 at $T = 4.2$ K [29,30] (see Sec. V for more details). Until now, this condition has been fulfilled only in nanowires with a thickness of several tens of nanometers [7,31]. A first limitation for the employment of YBCO nanowires with such thicknesses as single-photon detectors derives from the shape of the current-voltage characteristics. Indeed, the IVCs of YBCO nanowires with thicknesses of several tens of nanometers are flux-flow-like (see Fig. 1) [22,32], presenting at most voltage switches in the resistive state (i.e., at currents well above the critical one) as a consequence of phase slips or of entry of Abrikosov vortices [33,34]. The high value of the thermal conductivity in YBCO, which is two orders of magnitude higher than in NbN [35], prevents self-heating effects that could bring the whole device from the superconducting state directly to the normal state. Indeed, the average differential resistance δR in the measured finite-voltage range of the IVCs is much lower than the resistance R_N of the nanowire, measured at the onset of the superconducting transition. Therefore, a photon event, independently of the detection mechanism which takes place, cannot drive the whole nanowire in the normal state since $\delta R \ll R_L$, preventing the proper redistribution of the bias current from the wire into the load. Another drawback in the employment of YBCO in SNSPDs comes from the impossibility to increase the sheet resistance of the nanowires by increasing the granularity of the films. This is because grain boundaries significantly reduce the critical current instead of increasing it (which happens for NbN): granular sub-100-nm-wide YBCO nanowires present J_C no higher than 2×10^6 A/cm^2 [36].

This complex scenario has been confirmed by our previous works [7,37], in which we have shown that 50-nm-thick YBCO nanowires, despite critical current densities J_C close to the depairing limit, are characterized by a typical flux-flow-like behavior in the full temperature range. They have shown a purely bolometric response under irradiation.

To overcome these limitations, one needs to employ ultrathin YBCO films. Indeed, in films with thickness $t \leqslant 15$ nm the YBCO resistivity increases [38–40]; therefore, the thermal conductivity, via the Wiedemann-Franz law, decreases. Nanowires patterned on these films can be characterized by a physics close to that describing NbN nanowires, giving rise to hysteretic IVCs. The issue is therefore to reduce the thickness of YBCO nanowires, keeping the superconducting properties as close as possible to the bulk material. Indeed, as a consequence of the chemical instability of this material, together with its extreme sensitivity to defects and disorder, a significant J_C drop may occur at thicknesses comparable to ξ, reducing the Joule heating in the nanowires and therefore the probability to get hysteretic IVCs. Previous attempts to realize ultrathin YBCO nanowires have led to critical currents for the sub-100-nm-wide bridges more than one order of magnitude lower than J_v: as a consequence, despite the small cross sections, the IVCs are still flux-flow-like [20], or they show voltage switches only in the resistive state [21].

The structure of this paper is as follows. In Secs. III and IV we present the structural and transport characterization of ultrathin YBCO films. We show that, despite the lack of PBCO encapsulation, commonly used to protect thin YBCO, the film properties are intrinsic of the material, confined at thicknesses of a few nanometers. In Sec. V we study Au-capped YBCO nanowires, with thickness down to 10 nm, to show that our nanopatterning procedure, already successfully used on 50-nm-thick nanowires [31], can preserve the superconducting properties also in ultrathin structures. These nanowires are used as reference structures for the maximal J_C value one can achieve at this thickness. Finally, in Sec. VI we focus on bare 10-nm-thick YBCO nanowires to show their potentialities as SNSPDs.

III. ULTRATHIN FILMS: GROWTH AND STRUCTURAL CHARACTERIZATION

We deposited YBCO films, with thicknesses from 50 down to 3 nm, on MgO (110) substrates by pulsed laser deposition (heater temperature of 760 °C, oxygen pressure of 0.7 mbar, energy density of $2\,\mathrm{J/cm^2}$). After the deposition, the films were slowly cooled down (cooling rate of 5 °C/min) at an oxygen pressure of 900 mbar to promote full oxidation of the YBCO chains. With this procedure, we have previously shown that 50-nm-thick YBCO films are slightly overdoped [41]. For each thickness, we have deposited two YBCO films: one with a 50-nm-thick Au capping layer, *in situ* sputtered after the YBCO deposition, and another without the protective layer.

A morphological and structural characterization was carried out using atomic force microscopy (AFM) and scanning electron microscopy (SEM) to establish the quality of the YBCO films. The films present smooth surfaces, characterized by the typical c-axis domains with three-dimensional (3D) spirals and an average roughness which is of the order of one atomic cell (see Supplemental Material, Sec. S1 [42]).

The structural properties were determined by x-ray diffraction (XRD) analysis with a four-circle Panalytical X'pert diffractometer with Cu K_α radiation using a hybrid Ge(220) monochromator and a PIXcel 3D detector matrix. Symmetric 2θ-ω scans show that the ultrathin films are highly crystalline and c axis oriented [see Fig. 2(a)]. The crystallographic quality of the films is confirmed by the presence of the interference fringes which are visible on both sides of the lowest-diffraction-order $(00n)$ YBCO Bragg peaks [see Fig. 2(b)] in films with thicknesses down to 20 nm. The thickness t was calculated, with an error of less than one atomic layer ($\sim$1 nm), by considering couples of adjacent maxima and using the relation $t = \lambda_{Cu}[2(\sin\omega_n - \sin\omega_{n-1})]^{-1}$ (where $\omega_n = 2\theta_n/2$ are the angles corresponding to the maxima of the interference fringes and $\lambda_{Cu} = 1.540598$ Å is the wavelength of the incident x-ray wave).

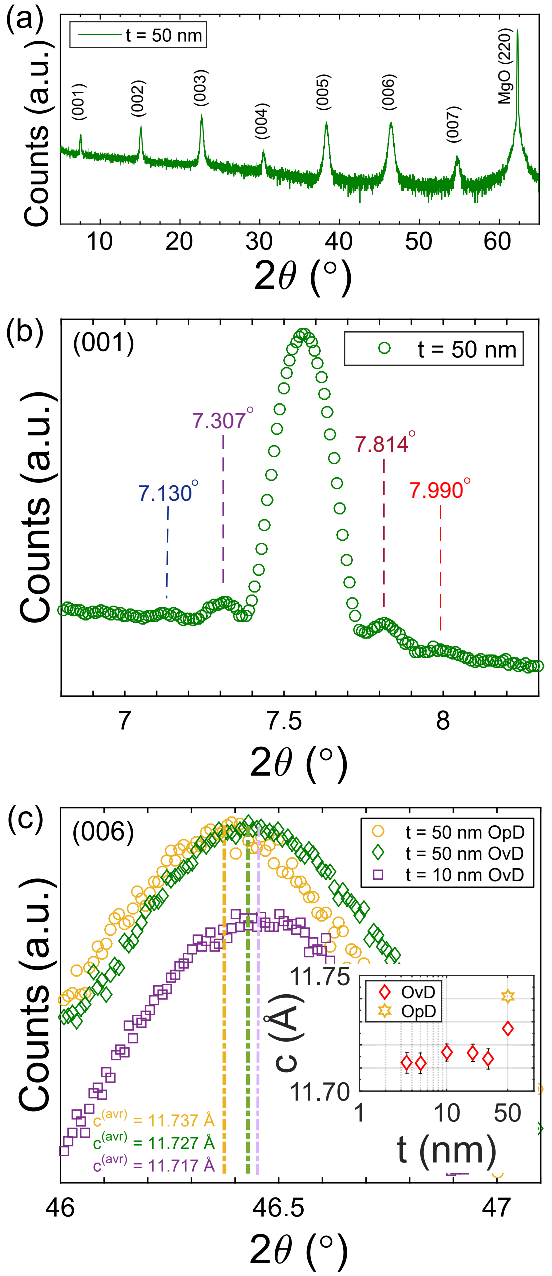

FIG. 2. (a) 2θ-ω x-ray diffraction scan of a 50-nm-thick slightly overdoped (OvD) YBCO film. (b) 2θ-ω XRD scan of the (001) Bragg reflection. (c) 2θ-ω XRD scans of the (006) reflections of 10-nm-thick (violet squares) and 50-nm-thick (green diamonds) slightly overdoped YBCO films. A 50-nm-thick nearly optimal doped YBCO film, obtained by using a reduced annealing oxygen pressure [41], is also shown for comparison (OpD, orange circles). The error bars are within the experimental points in all cases. The maximum of each peak is highlighted by the dashed line. The c-axis average values $c^{(\mathrm{avr})}$, extracted considering all the $(00n)$ reflections measured for the three films, are also reported. In the inset, $c^{(\mathrm{avr})}$ is plotted as a function of the film thickness.

From the angular position of the $(00n)$ peaks we can estimate the c-axis length. On the basis of the bulk lattice parameters of YBCO and MgO (110), a large in-plane lattice mismatch δ^m (defined as $|a_{\mathrm{sub}} - a_{\mathrm{film}}|/a_{\mathrm{sub}}$) is expected between the films and the substrate (δ^m is $\sim$9% and $\sim$35% along the [001] and [1 −1 0] MgO directions, respectively) [43]. In ultrathin YBCO films, especially when grown on substrates with a large mismatch, a *c*-axis expansion has usually been reported [44] and attributed to a large number of misfit dislocations caused by the extreme strain induced by the substrate on the whole film thickness. However, in our films, in spite of the large mismatch between the films and the substrates, no *c*-axis expansion is measured. In more detail, our films show a *c*-axis length of $\sim$11.715 Å, which is sizably smaller than those we have measured in optimally doped films grown on MgO (110) substrates, corresponding to $\sim$11.74 Å [see Fig. 2(c) and the inset therein]. Interestingly, films below 30-nm thickness have a slightly shorter *c* axis (i.e., 11.705 Å) than the reference slightly overdoped 50-nm-thick films [see Fig. 2(c) and the inset therein]. Such a small difference, compatible with a higher oxygen content, might be related to the efficiency of the postannealing in incorporating oxygen in films of only a few unit cells.

Cross-sectional high-resolution transmission electron microscopy (TEM) and high-angle annular dark-field scanning TEM (HAADF-STEM) investigations performed on 10-nm-thick films unveiled a complex nanostructure of the films characterized by a high density of $Y_2Ba_4Cu_8O_{16}$ (Y248) intergrowths intercalating within the YBCO matrix. Figure 3(a) shows a high-resolution *Z*-contrast image of the YBCO film in which the presence of Y248 planar faults is observed (indicated by arrows). In particular, as highlighted in the enlarged image [see Fig. 3(b)], the Y248 intergrowths are sometimes accompanied by a rigid shift of half the unit cell along the *b* axis of YBCO; hence, one can easily identify the [010] and [100] zone axes of the Y248 structure as a consequence of YBCO twinning. As a result of the presence of a high concentration of intergrowths, a waving of the (00ℓ) planes is observed with a consequent break in the vertical coherence which extends over the whole film thickness. The same nanostructural assessment is observed in the case of the 50-nm-thick films (not shown here). The presence of Y248 planar faults in YBCO thin films has been previously reported [45].

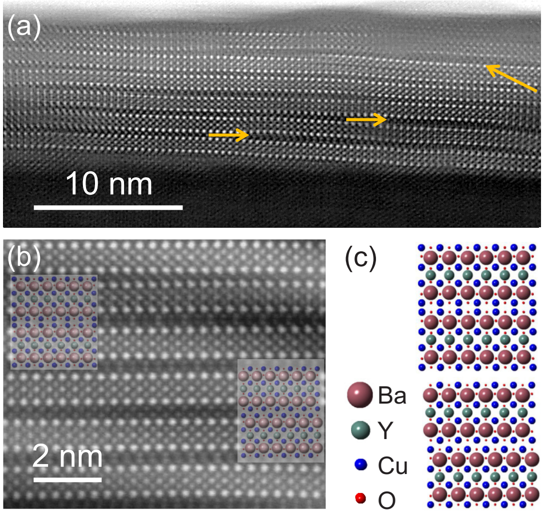

FIG. 3. (a) Atomic resolution HAADF-STEM image of a representative cross-sectional region of a 10-nm-thick film of YBCO. The presence of Y248 intergrowths is highlighted by arrows. (b) Close-up view showing the [010] and [100] zone axes of the Y248 crystal structure. (c) The two orientations of the Y248 cell, which are superimposed on the relative areas in (b).

The Y248 intergrowths introduce additional CuO chains into the structure, making our thin films Cu rich and overdoped at all thicknesses. This latter characteristic has been additionally confirmed by a transport characterization of the films, as will be discussed in the next section.

IV. ULTRATHIN FILMS: TRANSPORT CHARACTERIZATION

Transport properties of the ultrathin YBCO films have been studied using resistance vs temperature $R(T)$ measurements. For ultrathin YBCO films grown on substrates with a large mismatch (without a PBCO seed layer), a strong reduction of the zero-resistance temperature T_C^0 has been reported [46]. Here, we show instead that the T_C^0 of our films is higher than the liquid-nitrogen temperature down to thicknesses of 10 nm. From the onset of the superconducting transition and the normal-state properties of the ultrathin films we are able to extract information about the oxygen doping of nanometer-thick YBCO films.

A. Determination of the oxygen doping

In Figs. 4(a) and 4(b) the $R(T)$ measurements of the bare 10- and 20-nm-thick films are compared with those of the 50-nm-thick film (also without Au capping).

The onset temperature of the superconducting transition T_C^{onset} slightly changes with the film thickness [see inset table in Fig. 4(a)], while T_C^0 substantially decreases with reducing the thickness [due to the significant broadening of the superconducting transition; see Fig. 4(a)].

In principle a lower T_C^{onset} could be associated with both an increase and a reduction of the oxygen doping within the film. In our case, we can attribute the T_C^{onset} reduction to better oxygenation of the ultrathin films. This is clear from the normal-state $R(T)$ dependence of these films [see Fig. 4(b)] and from the comparison with $R(T)$ of an optimally doped 50-nm-thick film [see inset of Fig. 4(a)].

The optimally doped films are characterized by a linear behavior of the resistance as a function of the temperature in the full temperature range down to T_C^{onset}, as expected at this oxygen doping [47] [see inset of Fig. 4(a)]. The $R(T)$ measurements of the other three films are instead linear only at high temperature, while they exhibit a power-law dependence, with the same exponent $n = 1.2$, below a temperature $T \approx 200$ K. This behavior is typical of fully oxygenated YBCO films lying in the overdoped side of the phase diagram. The overdoped region of HTS materials is characterized by the so-called coherence temperature T_{coh} (a crossover temperature from a coherent and an incoherent metal state [48]), which increases as the oxygen doping increases: below T_{coh} the dependence of the resistance with the temperature is not linear

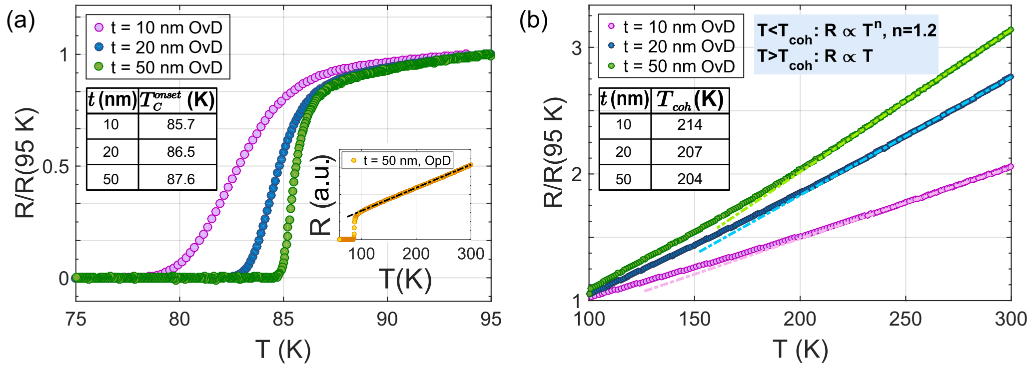

FIG. 4. (a) $R(T)$ curves, normalized to the value of the resistance at 95 K, of bare YBCO films with thicknesses $t = 10,20$, and 50 nm. The T_C^{onset} of the three films, listed in the inset table, are calculated as the temperature where the resistance $R = 0.9R_N$ (with R_N being the normal resistance). The inset shows the $R(T)$ measurement of a 50-nm-thick optimally doped bare YBCO film ($T_C^{\text{onset}} = 89.1$ K), which is linear down to ≈ 105 K. (b) Normalized resistance of the same three films as in (a) in the temperature range between 100 and 300 K. The dashed lines represent the linear fit to the data at temperatures close to 300 K. The linear dependence is in good agreement with the data down to T_{coh}. Below T_{coh}, the $R(T)$ data can be fitted assuming a power-law dependence $R = a + bT^n$, where a and b are free parameters and $n = 1.2$ for the three films. The resulting T_{coh} of the three films are listed in the inset table. The $R_\square$ values measured at 100 K in these three films are 130, 33, and 12 Ω, respectively, for $t = 10$, 20, and 50 nm.

any longer, and it becomes power-law-like, $R(T) = a + bT^n$. The exponent n varies from 1 at the optimal doping to 2 at the oxygen doping corresponding to the disappearance of the superconducting phase [47,49,50]. As shown in the inset table of Fig. 4(b), T_{coh} slightly increases by 10 K when the film thickness is reduced to 10 nm, signifying an oxygen content at least comparable to that of 50-nm-thick films, if not slightly higher than that.

The $R(T)$ of the films was measured with the Van der Pauw method [51] to extract the sheet resistance $R_\square$ and the resistivity $\rho = R_\square t$ and to determine their dependence on the film thickness. The resistivity is thickness independent in films down to 20 nm, with a value $\rho \approx 60\,\mu\Omega\,$cm at $T = 100$ K, which is comparable to that obtained from YBCO single crystals [52]. In 10-nm-thick films $\rho(100\text{ K})$ is instead $\sim$130 $\mu\Omega\,$cm: such an increase is expected since in the literature $R_\square$ is reported to scale faster than $1/t$ in sub-15-nm-thick films [38–40], where a significant drop in T_C^0 occurs (see the next section).

B. Broadening of the superconducting transition

In Fig. 5 we plot (red circles) the T_C^0 extracted by our YBCO films (bare films above $t = 10$ nm and Au-capped films below $t = 10$ nm) as a function of the thickness. As discussed earlier, T_C^0 slightly decreases down to 5 nm, which corresponds approximately to four unit cells. For lower thicknesses, it abruptly drops. Films with thickness of 3 nm, where only two complete atomic layers are present, are still superconducting with $T_C^0 = 14.5$ K. At even lower thicknesses the films are not superconducting down to 4.2 K.

We compare our results with those published in the literature starting from the beginning of the 1990s up to now. As previously mentioned, most of the works have focused on YBCO films sandwiched between two PBCO layers [12–14,39,53,54]. The T_C^0 values as a function of the YBCO thickness, collected from these papers, are shown as open symbols in Fig. 5. In all the previous works, T_C^0 gradually decreases down to four-unit-cell-thick ($t \approx 5$ nm) YBCO films while presenting a sudden drop at lower thicknesses. The same behavior can also be seen in superlattices when the YBCO layers are interchanged with either PBCO layers [55] or SrTiO$_3$ layers [56]. Below 5-nm-thick films, the spread of T_C^0 values which have been measured in different works becomes wider. The origin of this spread can have several possible reasons, related to an error in the determination of the thickness and/or to small differences between different samples (in the interdiffusion rate between Pr and Y atoms at the interfaces or in the PBCO stoichiometry and/or the presence of crystalline defects) [57].

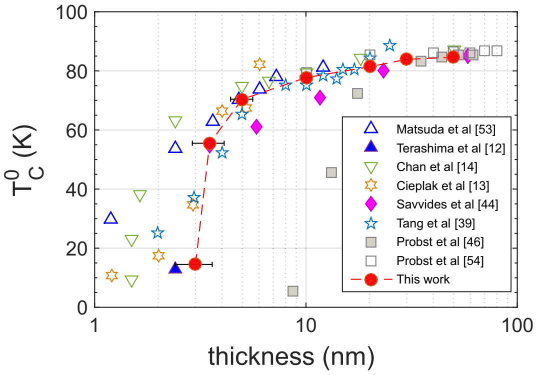

FIG. 5. Zero-resistance critical temperature T_C^0 of our capped and bare YBCO films versus their thickness (red circles). Our results are compared to those previously achieved in the literature. In particular, open symbols show results achieved on YBCO films sandwiched between two PBCO layers by Matsuda *et al.* [12,53], Chan *et al.* [14], Cieplak *et al.* [13], Tang *et al.* [39], and Probst *et al.* [54]. Solid symbols show instead results achieved on YBCO films not embedded between two PBCO layers by Terashima *et al.* [12], Savvides and Katsaros [44], and Probst *et al.* [46].

Our films (solid circles in Fig. 5), capped at most with a Au film, are characterized by T_C^0 values which are comparable, down to 5 nm, to the best results of PBCO/YBCO/PBCO multilayers (open triangles), while T_C^0 of the very thin films are the best reported values for bare YBCO structures.

The wide broadening of the superconducting transition (defined as $T_C^{\text{onset}} - T_C^0$), significantly suppressing T_C^0 of nanometer-size thin films, has been commonly attributed to an intrinsic size effect of the material and explained in terms of the Kosterlitz-Thouless (KT) transition related to vortex-antivortex pair dissociation in two-dimensional systems [53,58,59]. Even though such an interpretation has not achieved a general consensus [13,60], other mechanisms implicating transfer of charge carriers from the YBCO layer to the PBCO layer as well as the presence of structural defects at the PBCO/YBCO interfaces [57] can be ruled out in our case since we are dealing with bare YBCO films (or films capped with Au for thicknesses below 10 nm).

A second scenario which could explain both the drop in T_C^0 and the increase in resistivity exhibited by the ultrathin films points toward an increased disorder level in these systems near the superconductor-insulator transition. To quantify the degree of disorder in our YBCO films as a function of the thickness, the product of the Fermi wave vector k_F and electronic mean free path ℓ is commonly used [61]. In YBCO, $k_F = 1.2 \times 10^9\ \text{m}^{-1}$, while ℓ can be determined from the Drude model as $\ell = \hbar^2 v_F (\hbar\omega_P)^{-2} (\epsilon_0 \rho)^{-1}$, where $v_F = 1.4 \times 10^5\ \text{m}\,\text{s}^{-1}$ is the Fermi velocity, $\hbar\omega_P = 1.1$ eV is the plasma frequency [62], and ϵ_0 is the vacuum permittivity. In the 10-nm-thick films, as a consequence of the increase in resistivity, the $k_F\ell$ product drops from ~11.5, the value of all the thicker films, to ~5.3. In other superconductors, such as NbN, similar $k_F\ell$ values have been associated with a moderate disorder where a weakening of the pairing interactions is present but the role of phase fluctuation is still very limited [63]. The disorder becomes much stronger, and the phase fluctuations acquire a dominant role in films with thickness $t < 10$ nm. Here, we cannot make a quantitative study since the measured resistivities are dominated by the Au shunt. However, if we consider the same $\rho(t)$ dependence previously measured in other works [38], the $k_F\ell$ products are expected to drop even further, and the films are expected to be on the edge of a superconductor-insulator transition ($k_F\ell \approx 1$). According to the latter scenario, the YBCO films with thickness $t \leqslant 10$ nm are characterized by the same effective disorder, i.e., by the same $k_F\ell$ products, as NbN films used for SNSPDs [64].

V. ULTRATHIN Au-CAPPED NANOWIRES: PRISTINE NANOSTRUCTURES

Nanowires with widths down to 65 nm were fabricated [see Fig. 6(a)] using 10- and 20-nm-thick slightly overdoped YBCO films both with and without Au capping via a gentle Ar$^+$ ion milling through an *e*-beam lithography defined hard-carbon mask (for more details on the nanopatterning procedure, see Refs. [23,24]). The edges between the wires and the wider electrodes were designed with a rounded shape to minimize current crowding effects, which could be a source of reduction of the critical current density J_C [31,65].

The nanodevices were characterized via current-voltage characteristics (IVCs) and resistance versus temperature $R(T)$ measurements. We have compared the results with those obtained for nanowires with the same geometry obtained on 50-nm-thick YBCO films capped with Au that we use as a reference [23,24].

All the measured nanowires were superconducting. The IVCs of the nanowires at $T = 4.2$ K exhibit a typical flux-flow-like behavior. From the IVCs we can determine the critical current I_C of the nanowires, and the critical current density $J_C = I_C/(wt)$, where w is the width of the nanowire.

To test the reproducibility of our nanostructures, we measured for each sample a large number Π of identical wires. Figure 6(b) shows the normal profile, determined by the distribution of the extracted J_C values, as a function of the film thickness. For each distribution, we can extract an average critical current density $\bar{J}_C$. The J_C distributions become broader for thinner nanowires, possibly due to a very prominent role of defects at such reduced dimensions. However, $\bar{J}_C$ is the same as for the 50-nm-thick nanowires, and the highest J_C within each distribution is $J_C^{\max} \approx 8 \times 10^7\ \text{A/cm}^2$. For nanowires which are characterized by dimensions $w,l \gg 4.44\xi_0$ (where $\xi_0 \approx 2$ nm for YBCO is the superconducting coherence length at zero temperature), the maximum J_C is given by the entry of Abrikosov vortices, driven by the Lorentz force, overcoming the bridge edge barrier. In this regime J_v (critical current density due to vortex entry) can approximately be written as [29,30]

$$J_v \approx 0.826 J_d, \tag{1}$$

where J_d is the depairing critical current density, predicted by the Ginzburg-Landau theory, whose expression [66]

$$J_d = \frac{\Phi_0}{3^{3/2}\pi\mu_0\lambda_0^2\xi_0} \tag{2}$$

equals to $1\text{–}3 \times 10^8\ \text{A/cm}^2$ for YBCO nanowires [23,24,31]. In Eq. (2), Φ_0 is the flux quantum, μ_0 is the vacuum permeability, and λ_0 is the London penetration depth at zero temperature. The maximum J_C value of our nanostructures is therefore close to the theoretical limit, showing that superconducting properties close to the as-grown films are preserved even at ultrathin thicknesses.

The resistance as a function of the temperature close to the transition is shown in Fig. 6(c) for three nanowires, with thicknesses $t = 10, 20$, and 50 nm. For each device, the first transition in $R(T)$, at higher temperature, is related to the wide electrodes connected to the nanowire: the temperature range of this transition corresponds to that of the unpatterned film [seen in Fig. 4(a)], although the onset $T_{C,e}^{\text{onset}}$ is lower because of the shunt effect of the Au layer [23]. The second, broader transition in $R(T)$, at lower temperature, is instead associated with the nanowire: what is more remarkable about this transition is that the onset temperature $T_{C,w}^{\text{onset}}$ is typically only 1–2 K lower than that of the wide electrodes $T_{C,e}^{\text{onset}}$, independent of the thickness.

The broadening of the superconducting transition of the thinnest nanowires is not much wider than that of the 50-nm-thick nanowires. However, this broadening cannot be ascribed only to the dissipation induced by Abrikosov vortices crossing the nanowires, shown for the 50-nm-thick nanodevices in other

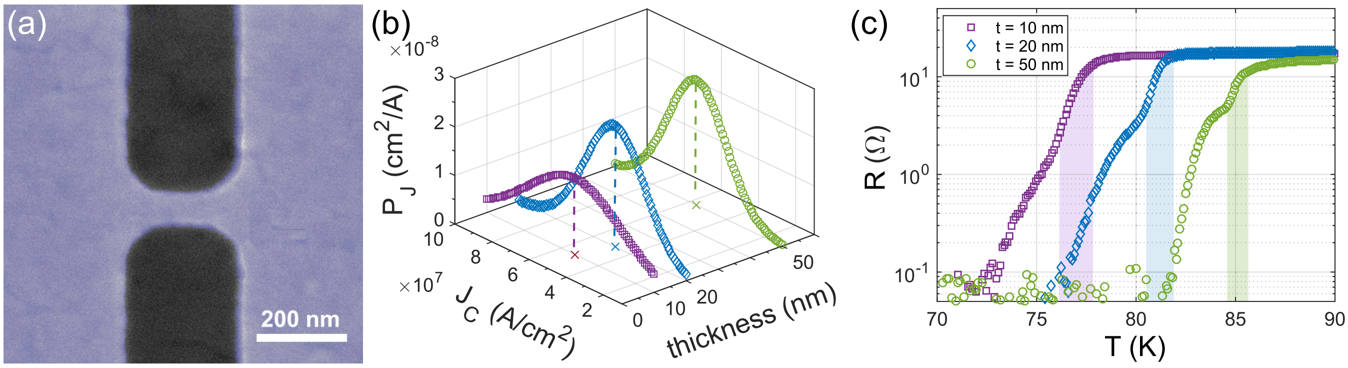

FIG. 6. (a) Scanning electron microscopy picture of a Au-capped 10-nm-thick and 65-nm-wide YBCO nanowire. (b) Distribution P_J of the critical current densities J_C at $T = 4.2$ K of the population Π of 65-nm-wide Au-capped nanowires as a function of the wire thickness ($\Pi_{10nm} = 12$, $\Pi_{20nm} = 59$, and $\Pi_{50nm} = 18$). The $\bar{J}_C$ values of the three distributions, highlighted by the dashed lines, are almost identical ($\bar{J}_{C\,10nm} = 5.3 \times 10^7$ A/cm^2, $\bar{J}_{C\,20nm} = 4.8 \times 10^7$ A/cm^2, and $\bar{J}_{C\,50nm} = 5.6 \times 10^7$ A/cm^2). (c) $R(T)$ of three 65-nm-wide Au-capped nanowires at different thicknesses. The shaded areas represent the temperature intervals between $T_{C,w}^{\text{onset}}$ and $T_{C,e}^{\text{onset}}$.

works [30,67,68]. Indeed, for ultrathin nanowires the picture is more complicated since the broadening due to the thickness confinement, related to the various mechanisms mentioned in the previous section, including the KT transition, valid for 2D superconductors [58], has to be taken into account. Thus, a quantitative analysis of the superconducting transition of ultrathin nanowires requires further investigations, which go beyond the scope of this paper.

VI. ULTRATHIN BARE NANOWIRES: A POSSIBLE PLATFORM FOR YBCO SINGLE-PHOTON DETECTORS

For most applications requiring ultrathin superconducting devices, a Au capping layer is not ideal. For single-photon detection applications, for example, the high conductivity of Au leads to a high reflection of the light. At the same time, the Au capping layer works as an electrical shunt for the photoresponse and could also represent a thermal shunt for the perturbed area/hot spot inside the detector [7].

The occurrence of hysteretic IVCs, associated with the formation of a self-stabilizing hot spot in a superconducting nanowire, is not very likely to happen in YBCO nanowires. As already mentioned in Sec. II, this is mainly because of the high value of the thermal conductivity κ in YBCO, in particular close to the optimally doped regime [35] ($\kappa \approx 15\,\mathrm{W\,m^{-1}\,K^{-1}}$ in the normal state), preventing self-heating effects that could turn normal the central part of the nanowire.

Here, we present the fabrication of bare YBCO nanowires, patterned on 10-nm and 20-nm-thick films such as those discussed in Secs. III and IV. With respect to the nanofabrication procedure described in other works [23,24], a hard-carbon mask, deposited by pulsed laser deposition at room temperature and removed at the end of the nanopatterning by oxygen plasma etching, was the only protective capping layer for the YBCO film during the nanopatterning [69]. The carbon layer protects YBCO from chemicals and from the direct impact of the Ar$^+$ ions during the etching. Because of its low thermal conductivity, it is not as effective as Au in preventing heating of YBCO during the baking of the resists and during the ion milling. This may lead to possible deoxygenation from the nanowire sidewalls during the nanopatterning and the occurrence of some randomly distributed inhomogeneities.

Transport measurements were done on 20-nm-thick bare YBCO nanowires, characterized by resistivity values very close to those of 50-nm-thick wires. From the IVCs at $T = 4.2$ K of the nanostructures, we have extracted J_C up to 5×10^7 A/cm^2, the average critical current density of the reference Au-capped nanowires (see Sec. V). However, a voltage switch from the superconducting to the normal state has never been observed.

In the following we show that bare nanowires, with thickness $t = 10$ nm, are instead characterized, similar to NbN nanowires, by hysteretic IVCs, with a voltage switch driving the structures abruptly from the superconducting to the normal state as soon as the critical current is exceeded. Current-voltage characteristics and resistance versus temperature measurements were carried out on 38 nanowires with widths in the range 65–120 nm and lengths in the range 100–500 nm and patterned on several 10-nm-thick films.

From the IVCs, measured at $T = 4.2$ K in the current bias mode, we have inferred critical current densities as high as $J_C \approx 3.5 \times 10^7$ A/cm^2, quite close to the average critical current density of the Au-capped nanowires (which are reference nanowires). As a consequence of the choice of carbon as a capping layer, we have obtained only a slightly lower $\bar{J}_C$, but with a larger spread of J_C values (see Supplemental Material, Sec. S2 [42]), and broader resistive transitions compared with nanowires capped with Au [see Fig. 7(b)].

The IVCs of the nanowires with J_C lower than $\sim 5 \times 10^6$ A/cm^2 are flux-flow-like (see Supplemental Material, Sec. S2 [42]). The shape of the IVCs instead abruptly changes for nanowires with J_C higher than this threshold. A large voltage switch, of the order of several millivolts, appears above I_C, which drives the devices to a state characterized by a constant differential resistance, $dV/dI \approx 1$–$4 \times 10^2\,\Omega$, up to $V \approx 20$ mV when applying a bias current $I_b > I_C$ [see Fig. 7(a)]. The difference between the switching (I_C) and retrapping (I_r) currents is on the order of several microamperes. The fact that we observe the voltage switch only in nanowires with the highest J_C, approaching the maximum current density

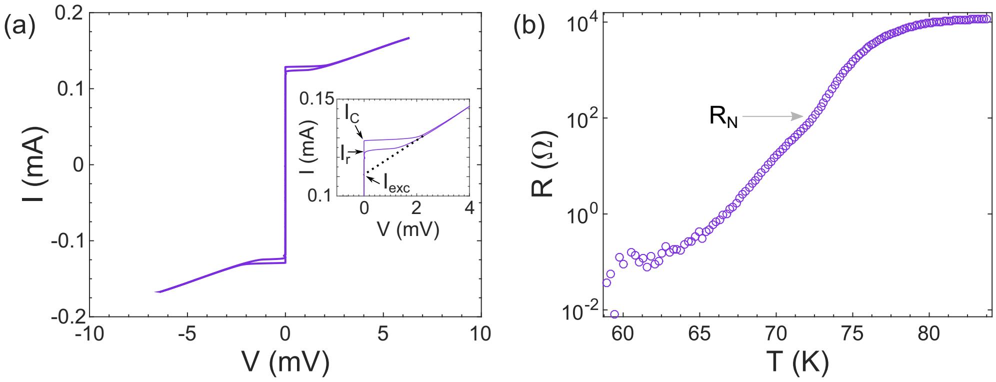

FIG. 7. (a) The IVC measured at $T = 4.2$ K of a 75-nm-wide and 100-nm-long bare nanowire ($J_C = 1.8 \times 10^7$ A/cm^2) presents a 2-mV-wide voltage switch above I_C, which drives the system to the normal state, corresponding to a differential resistance $dV/dI = 112\ \Omega$ (see inset). The IVC presents an excess current I_{exc}, possibly deriving from Andreev reflections at the interface between the superconductor and the normal region originating from a hot spot [70]. (b) $R(T)$ measurement of the same nanowire. The value of the normal resistance, corresponding to T_C^{onset} of the nanowire, is $R_N \approx 100\ \Omega$, very close to the dV/dI value measured in the IVC.

a YBCO nanowire can carry, is an indication that the switching is not caused by the presence of local grain boundaries or defects.

The normal resistance R_N (the value of the resistance at the onset of the superconducting transition) of the nanowires is very close to the differential resistance dV/dI measured in the IVCs at 4.2 K in all the investigated samples [see Fig. 7(b)], in agreement with what is observed in NbN nanowires (see Fig. 1). This occurrence supports the hypothesis that the voltage switch above I_C is a sign of self-heating in the nanowires: a normal/conducting domain, induced inside the ultrathin wire, drives the system directly from the superconducting to the normal state. This hypothesis is further supported by the presence of excess current in the hysteretic IVCs of the nanowires, again in accordance with results for NbN nanowires (see Fig. 1). The excess current, corresponding to the extrapolation to zero voltage of the normal branch at high bias, derives from Andreev reflections at the two interfaces between the superconductor and the normal region originating from a self-stabilizing hot spot [70].

It is worth mentioning that the self-heating hot-spot model is simplistic, and it is not meant to describe the detection mechanism in these nanowires: in type-II superconductors, like NbN and YBCO, magnetic vortices play an important role (as already highlighted in Sec. V) [29]; in addition to this, the physics of ultrathin films and nanowires is characterized by thermal and quantum phase slips [71,72]. Nevertheless, NbN nanowires still work as SNSPDs whether their physics is dominated by phase slips or vortices [4,73]. The understanding of the processes responsible for the formation and development of the normal/conducting domain within our nanowires upon irradiation goes beyond the purpose of the present paper.

Qualitatively, within the simplistic framework of the self-heating hot-spot model [74], which recently has even been used to describe the IVCs of NbN [26,75,76] and cuprate HTS [77,78] nanowires, the central part of the wire becomes normal due to Joule heating, producing a power equal to IV. A cooling mechanism follows via phonons and electron diffusion. The occurrence of the switch in the IVCs of 10-nm-thick wires might be related to the increase in the film resistivity in YBCO below 15 nm [38–40]. As mentioned in Sec. IV, in our 10-nm-thick nanowires we have measured at T_C a resistivity ρ which is more than a factor of 2 higher than the ρ of our 50- and 20-nm-thick nanowires. Indeed, an increase in resistivity would result in an increase of Joule heating, while at the same time the thermal conductivity κ is decreased via the Wiedemann-Franz law, $\kappa(T) = \mathcal{L}T/\rho$, where $\mathcal{L} = \pi^2 k_B^2/3e^2 \approx 2.45 \times 10^{-8}\ \mathrm{W}\,\Omega/\mathrm{K}^2$ is the Lorentz number. Both factors would support the stabilization of a hot spot in our ultrathin nanowires. It is worth mentioning that in NbN wires, the value of the retrapping current I_r, which within the self-heating hot-spot model depends on the ρ of the material, on the thickness, and on the thermal coupling between the wire and the substrate, has been experimentally found to decrease with decreasing thickness [76]. This implies that the stabilization of a hot spot is favored in ultrathin wires.

Finally, we have measured the IVCs of the 10-nm-thick bare YBCO nanowires as a function of the temperature up to T_C: the switching current I_C decreases more rapidly than the retrapping current I_r when increasing the temperature, leading to a gradual narrowing of the hysteresis (see Fig. 8). In

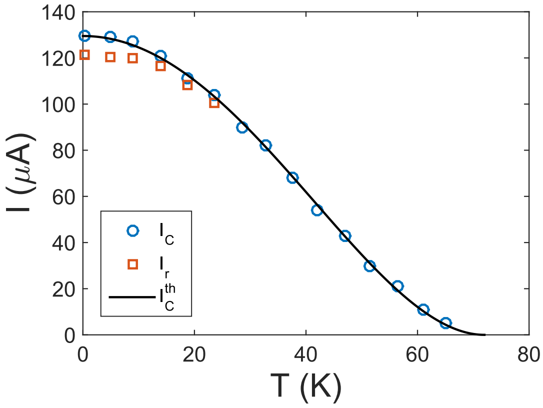

FIG. 8. Experimental critical current I_C (circles) and retrapping current I_r (squares) as a function of the temperature for the nanowire shown in Fig. 7. The solid line is a guide for the eye.

particular, the hysteresis is almost negligible if $T > 0.4T_C$. In NbN nanowires the hysteresis, which also decreases with increasing temperature [79], can instead persist up to temperatures close to T_C. In our case, the narrower T/T_C range in which $I_C > I_r$ might be due to the smaller value of κ of YBCO with respect to that of NbN. This is also evident from the shape of the IVCs at $T = 4.2$ K, presenting hysteresis, i.e., values of the retrapping voltage and difference between I_C and I_r much smaller than those of NbN nanowires (see Fig. 1).

VII. SUMMARY AND CONCLUSIONS

We have shown the realization of YBCO films which exhibit superconductivity down to 3 nm. The films show a c axis, close to the reference 50-nm-thick films, still corresponding to a slightly overdoped regime and signifying a high crystallinity down to two to three unit cells. Moreover, the T_C^0 of the thinnest films, obtained by using Au capping, is comparable, down to four unit cells, to the best value obtained by sandwiching YBCO films with PBCO. Since the presence of the PBCO capping and buffering induces substitutions and/or chemical modifications, our results can be considered a first step toward the realization of few-unit-cell structures with properties representative of the YBCO bulk.

We have also fabricated YBCO nanowires with thicknesses down to 10 nm and widths down to 65 nm, both with and without the protection of a Au capping layer. The ultrathin Au-capped YBCO nanowires ($t = 10$ nm) behave similarly to the 50-nm-thick nanowires and are characterized by superconducting properties not affected by the nanopatterning procedure up to their T_C^0, a value close to the T_C^0 of the unpatterned films. The IVCs are nonhysteretic. The ultrathin 10-nm-thick bare YBCO nanowires are instead characterized by hysteretic current-voltage characteristics, with a voltage switch of the order of a few millivolts from the superconducting to the normal state. In addition to this bistability of the IVCs around I_C, in our bare nanowires coexist (1) very small cross sections with sub-100-nm widths and thicknesses not far from the superconducting coherence length; (2) high critical current densities, approaching the critical depairing value, limited by vortex entry; and (3) enhanced sheet resistances, expected in sub-15-nm-thick films and nanostructures, which make it possible to engineer sub-micrometer-long wires with $k\Omega$ resistance values which are much larger than the 50 Ω resistance used in parallel with the device in high-speed SNSPD readout circuits. The coexistence of these four features makes our ultrathin YBCO nanowires very attractive for SNSPDs.

ACKNOWLEDGMENT

This work has been partially supported by the Swedish Research Council (VR) and the Knut and Alice Wallenberg Foundation.

---

[1] G. Gol'tsman, O. Okunev, G. Chulkova, A. Lipatov, A. Semenov, K. Smirnov, B. Voronov, A. Dzardanov, C. Williams, and R. Sobolewski, Appl. Phys. Lett. **79**, 705 (2001).

[2] F. Marsili, F. Najafi, E. Dauler, F. Bellei, X. Hu, M. Csete, R. J. Molnar, and K. K. Berggren, Nano Lett. **11**, 2048 (2011).

[3] C. M. Natarajan, M. G. Tanner, and R. H. Hadfield, Supercond. Sci. Technol. **25**, 063001 (2012).

[4] A. Engel, J. Renema, K. Il'in, and A. Semenov, Supercond. Sci. Technol. **28**, 114003 (2015).

[5] R. Sobolewski, Proc. SPIE **3481**, 480 (1998).

[6] L. Parlato, R. Arpaia, C. De Lisio, F. M. Granozio, G. Pepe, P. Perna, V. Pagliarulo, C. Bonavolonta, M. Radovic, Y. Wang *et al.*, Phys. Rev. B **87**, 134514 (2013).

[7] R. Arpaia, M. Ejrnaes, L. Parlato, F. Tafuri, R. Cristiano, D. Golubev, R. Sobolewski, T. Bauch, F. Lombardi, and G. Pepe, Physica C (Amsterdam, Neth.) **509**, 16 (2015).

[8] M. Lyatti, A. Savenko, and U. Poppe, Supercond. Sci. Technol. **29**, 065017 (2016).

[9] G. Balestrino and A. Tebano, Supercond. Sci. Technol. **16**, R29 (2003).

[10] J.-M. Triscone, M. G. Karkut, L. Antognazza, O. Brunner, and Ø. Fischer, Phys. Rev. Lett. **63**, 1016 (1989).

[11] Q. Li, X. X. Xi, X. D. Wu, A. Inam, S. Vadlamannati, W. L. McLean, T. Venkatesan, R. Ramesh, D. M. Hwang, J. A. Martinez, and L. Nazar, Phys. Rev. Lett. **64**, 3086 (1990).

[12] T. Terashima, K. Shimura, Y. Bando, Y. Matsuda, A. Fujiyama, and S. Komiyama, Phys. Rev. Lett. **67**, 1362 (1991).

[13] M. Z. Cieplak, S. Guha, S. Vadlamannati, T. Giebultowicz, and P. Lindenfeld, Phys. Rev. B **50**, 12876 (1994).

[14] I. Chan, D. Vier, O. Nakamura, J. Hasen, J. Guimpel, S. Schultz, and I. K. Schuller, Phys. Lett. A **175**, 241 (1993).

[15] A. Semenov, B. Günther, U. Böttger, H.-W. Hübers, H. Bartolf, A. Engel, A. Schilling, K. Ilin, M. Siegel, R. Schneider *et al.*, Phys. Rev. B **80**, 054510 (2009).

[16] J. Kitaygorsky, I. Komissarov, A. Jukna, D. Pan, O. Minaeva, N. Kaurova, A. Divochiy, A. Korneev, M. Tarkhov, B. Voronov *et al.*, IEEE Trans. Appl. Supercond. **17**, 275 (2007).

[17] H. Bartolf, A. Engel, A. Schilling, K. Il'in, M. Siegel, H.-W. Hübers, and A. Semenov, Phys. Rev. B **81**, 024502 (2010).

[18] J. Renema, R. Gaudio, Q. Wang, Z. Zhou, A. Gaggero, F. Mattioli, R. Leoni, D. Sahin, M. De Dood, A. Fiore *et al.*, Phys. Rev. Lett. **112**, 117604 (2014).

[19] G. Blatter, M. V. Feigel'man, V. B. Geshkenbein, A. I. Larkin, and V. M. Vinokur, Rev. Mod. Phys. **66**, 1125 (1994).

[20] N. Curtz, E. Koller, H. Zbinden, M. Decroux, L. Antognazza, Ø. Fischer, and N. Gisin, Supercond. Sci. Technol. **23**, 045015 (2010).

[21] M. Lyatti, A. Savenko, U. Poppe, and R. Dunin-Borkowski, arXiv:1603.03459.

[22] P. Amari, C. Feuillet-Palma, A. Jouan, F. Couedo, N. Bourlet, E. Géron, M. Malnou, L. Méchin, A. Sharafiev, J. Lesueur *et al.*, arXiv:1612.07730.

[23] R. Arpaia, S. Nawaz, F. Lombardi, and T. Bauch, IEEE Trans. Appl. Supercond. **23**, 1101505 (2013).

[24] S. Nawaz, R. Arpaia, T. Bauch, and F. Lombardi, Physica C (Amsterdam, Neth.) **495**, 33 (2013).

[25] K. Il'in, M. Siegel, A. Semenov, A. Engel, and H.-W. Hübers, Phys. Status Solidi C **2**, 1680 (2005).

[26] A. Stockhausen, K. Il'in, M. Siegel, U. Södervall, P. Jedrasik, A. Semenov, and H. Hübers, Supercond. Sci. Technol. **25**, 035012 (2012).

[27] V. Yurchenko, K. Ilin, J. Meckbach, M. Siegel, A. Qviller, Y. Galperin, and T. H. Johansen, Appl. Phys. Lett. **102**, 252601 (2013).

[28] S.-Z. Lin, O. Ayala-Valenzuela, R. D. McDonald, L. N. Bulaevskii, T. G. Holesinger, F. Ronning, N. R. Weisse-Bernstein, T. L. Williamson, A. H. Mueller, M. A. Hoffbauer *et al.*, Phys. Rev. B **87**, 184507 (2013).

[29] L. N. Bulaevskii, M. J. Graf, C. D. Batista, and V. G. Kogan, Phys. Rev. B **83**, 144526 (2011).

[30] R. Arpaia, D. Golubev, R. Baghdadi, M. Arzeo, G. Kunakova, S. Charpentier, S. Nawaz, F. Lombardi, and T. Bauch, Physica C (Amsterdam, Neth.) **506**, 165 (2014).

[31] S. Nawaz, R. Arpaia, F. Lombardi, and T. Bauch, Phys. Rev. Lett. **110**, 167004 (2013).

[32] G. Papari, F. Carillo, D. Stornaiuolo, D. Massarotti, L. Longobardi, F. Beltram, and F. Tafuri, Physica C (Amsterdam, Neth.) **506**, 188 (2014).

[33] H. Assink, A. Harg, C. Schep, N. Chen, D. Marel, P. Hadley, E. Drift, and J. Mooij, IEEE Trans. Appl. Supercond. **3**, 2983 (1993).

[34] P. Mikheenko, X. Deng, S. Gildert, M. S. Colclough, R. A. Smith, C. M. Muirhead, P. D. Prewett, and J. Teng, Phys. Rev. B **72**, 174506 (2005).

[35] M. Sutherland, D. G. Hawthorn, R. W. Hill, F. Ronning, S. Wakimoto, H. Zhang, C. Proust, E. Boaknin, C. Lupien, L. Taillefer, R. Liang, D. A. Bonn, W. N. Hardy, R. Gagnon, N. E. Hussey, T. Kimura, M. Nohara, and H. Takagi, Phys. Rev. B **67**, 174520 (2003).

[36] D. Levi, A. Shaulov, A. Frydman, G. Koren, B. Y. Shapiro, and Y. Yeshurun, Europhys. Lett. **101**, 67005 (2013).

[37] R. Arpaia, M. Ejrnaes, L. Parlato, R. Cristiano, M. Arzeo, T. Bauch, S. Nawaz, F. Tafuri, G. Pepe, and F. Lombardi, Supercond. Sci. Technol. **27**, 044027 (2014).

[38] J. Gao, W. Wong, and J. Xhie, Appl. Phys. Lett. **67**, 2232 (1995).

[39] W. Tang, C. Ng, C. Yau, and J. Gao, Supercond. Sci. Technol. **13**, 580 (2000).

[40] U. Poppe, N. Klein, U. Dähne, H. Soltner, C. Jia, B. Kabius, K. Urban, A. Lubig, K. Schmidt, S. Hensen *et al.*, J. Appl. Phys. **71**, 5572 (1992).

[41] R. Baghdadi, R. Arpaia, T. Bauch, and F. Lombardi, IEEE Trans. Appl. Supercond. **25**, 1100104 (2015).

[42] See Supplemental Material at http://link.aps.org/supplemental/10.1103/PhysRevB.96.064525 for details on the film morphology and on the current-voltage characterization of a set of ultrathin bare nanowires.

[43] X.-Y. Zheng, D. H. Lowndes, S. Zhu, J. D. Budai, and R. J. Warmack, Phys. Rev. B **45**, 7584 (1992).

[44] N. Savvides and A. Katsaros, Physica C (Amsterdam, Neth.) **226**, 23 (1994).

[45] R. Guzman, J. Gazquez, V. Rouco, A. Palau, C. Magen, M. Varela, J. Arbiol, X. Obradors, and T. Puig, Appl. Phys. Lett. **102**, 081906 (2013).

[46] P. Probst, K. Il'in, A. Engel, A. Semenov, H.-W. Hübers, J. Hänisch, B. Holzapfel, and M. Siegel, Physica C (Amsterdam, Neth.) **479**, 173 (2012).

[47] N. Hussey, J. Phys. Condens. Matter **20**, 123201 (2008).

[48] A. Kaminski, S. Rosenkranz, H. M. Fretwell, Z. Z. Li, H. Raffy, M. Randeria, M. R. Norman, and J. C. Campuzano, Phys. Rev. Lett. **90**, 207003 (2003).

[49] T. Manako, Y. Kubo, and Y. Shimakawa, Phys. Rev. B **46**, 11019 (1992).

[50] A. P. Mackenzie, S. R. Julian, D. C. Sinclair, and C. T. Lin, Phys. Rev. B **53**, 5848 (1996).

[51] L. J. Van der Pauw, Philips Res. Rep. **13**, 1 (1958).

[52] R. Liang, P. Dosanjh, D. Bonn, D. Baar, J. Carolan, and W. Hardy, Physica C (Amsterdam, Neth.) **195**, 51 (1992).

[53] Y. Matsuda, S. Komiyama, T. Onogi, T. Terashima, K. Shimura, and Y. Bando, Phys. Rev. B **48**, 10498 (1993).

[54] P. Probst, A. Semenov, M. Ries, A. Hoehl, P. Rieger, A. Scheuring, V. Judin, S. Wünsch, K. Il'in, N. Smale, Y.-L. Mathis, R. Müller, G. Ulm, G. Wüstefeld, H.-W. Hübers, J. Hänisch, B. Holzapfel, M. Siegel, and A.-S. Müller, Phys. Rev. B **85**, 174511 (2012).

[55] M. Varela, Z. Sefrioui, D. Arias, M. A. Navacerrada, M. Lucía, M. A. López de la Torre, C. León, G. D. Loos, F. Sánchez-Quesada, and J. Santamaría, Phys. Rev. Lett. **83**, 3936 (1999).

[56] J. Garcia-Barriocanal, A. M. Perez-Muñoz, Z. Sefrioui, D. Arias, M. Varela, C. Leon, S. J. Pennycook, and J. Santamaria, Phys. Rev. B **87**, 245105 (2013).

[57] M. Cieplak, S. Vadlamannati, S. Guha, C. Nien, and P. Lindenfeld, Physica C (Amsterdam, Neth.) **209**, 31 (1993).

[58] M. R. Beasley, J. E. Mooij, and T. P. Orlando, Phys. Rev. Lett. **42**, 1165 (1979).

[59] J.-M. Triscone and Ø. Fischer, Rep. Prog. Phys. **60**, 1673 (1997).

[60] J. M. Repaci, C. Kwon, Q. Li, X. Jiang, T. Venkatessan, R. E. Glover III, C. J. Lobb, and R. S. Newrock, Phys. Rev. B **54**, R9674 (1996).

[61] A. F. Ioffe and A. R. Regel, Prog. Semicond. **4**, 237 (1960).

[62] M. Gurvitch and A. T. Fiory, Phys. Rev. Lett. **59**, 1337 (1987).

[63] M. Chand, G. Saraswat, A. Kamlapure, M. Mondal, S. Kumar, J. Jesudasan, V. Bagwe, L. Benfatto, V. Tripathi, and P. Raychaudhuri, Phys. Rev. B **85**, 014508 (2012).

[64] A. Kozorezov, C. Lambert, F. Marsili, M. Stevens, V. Verma, J. Stern, R. Horansky, S. Dyer, S. Duff, D. Pappas *et al.*, Phys. Rev. B **92**, 064504 (2015).

[65] J. R. Clem and K. K. Berggren, Phys. Rev. B **84**, 174510 (2011).

[66] M. Tinkham, *Introduction to Superconductivity* (Dover Publications, New York, 2004).

[67] R. Arpaia, S. Charpentier, R. Toskovic, T. Bauch, and F. Lombardi, Physica C (Amsterdam, Neth.) **506**, 184 (2014).

[68] R. Baghdadi, R. Arpaia, S. Charpentier, D. Golubev, T. Bauch, and F. Lombardi, Phys. Rev. Appl. **4**, 014022 (2015).

[69] R. Arpaia, M. Arzeo, R. Baghdadi, E. Trabaldo, F. Lombardi, and T. Bauch, Supercond. Sci. Technol. **30**, 014008 (2017).

[70] G. E. Blonder, M. Tinkham, and T. M. Klapwijk, Phys. Rev. B **25**, 4515 (1982).

[71] M. Zgirski, K.-P. Riikonen, V. Touboltsev, and K. Arutyunov, Nano Lett. **5**, 1029 (2005).

[72] O. Astafiev, L. Ioffe, S. Kafanov, Y. A. Pashkin, K. Y. Arutyunov, D. Shahar, O. Cohen, and J. Tsai, Nature (London) **484**, 355 (2012).

[73] C. Delacour, B. Pannetier, J.-C. Villegier, and V. Bouchiat, Nano Lett. **12**, 3501 (2012).

[74] W. Skocpol, M. Beasley, and M. Tinkham, J. Appl. Phys. **45**, 4054 (1974).

[75] S. Adam, L. Piraux, S. Michotte, D. Lucot, and D. Mailly, J. Phys. Conf. Ser. **234**, 022001 (2010).

[76] E. Schmidt, K. Ilin, and M. Siegel, IEEE Trans. Appl. Supercond. **27**, 1 (2017).

[77] D. Golubev, F. Lombardi, and T. Bauch, Physica C (Amsterdam, Neth.) **506**, 174 (2014).

[78] S. Charpentier, R. Arpaia, J. Gaudet, D. Matte, R. Baghdadi, T. Löfwander, D. Golubev, P. Fournier, T. Bauch, and F. Lombardi, Phys. Rev. B **94**, 060503 (2016).

[79] S. Adam, L. Piraux, S. Michotte, D. Lucot, and D. Mailly, Supercond. Sci. Technol. **22**, 105010 (2009).